Flow induced by an oscillating sphere in probing complex viscosity of polymer solutions

Yanzhen He,[1] Lu Li,[1] Takashi Taniguchi,[2] Remco Tuinier,[3,4] and Tai-Hsi Fan[1,*]

[1]*Department of Mechanical Engineering, University of Connecticut, Storrs, Connecticut 06269, USA*

[2]*Department of Chemical Engineering, Kyoto University, Kyoto 615-8510, Japan*

[3]*Laboratory of Physical Chemistry, Department of Chemical Engineering and Chemistry & Institute for Complex Molecular Systems, Eindhoven University of Technology, P.O. Box 513, 5600 MB Eindhoven, The Netherlands*

[4]*Van't Hoff Laboratory for Physical and Colloid Chemistry, Debye Institute, Department of Chemistry, Utrecht University, The Netherlands*

(Received 17 January 2016; published 7 January 2020)

A theoretical investigation is presented for a linear viscoelastic flow induced by an oscillatory colloidal particle in nonadsorbing polymer solutions. At small-amplitude oscillations, the polymer distribution is assumed to be at equilibrium and forms a depletion zone around the particle based on the mean-field approximation. The goal of the theoretical approach is to predict the apparent complex viscosity sensed by the particle and compare this with the actual viscosity of the bulk fluid. Due to the local inhomogeneity, substantial deviation between the apparent and true viscosity in the bulk needs to be corrected quantitatively. The resulting apparent complex viscosity or friction coefficient in the Fourier domain will help to interpret active and passive microrheological measurements of colloid-polymer mixtures that take polymer depletion into account.

DOI: 10.1103/PhysRevFluids.5.013302

I. INTRODUCTION

Viscoelastic properties of complex fluids are fundamental concerns for many applications in food, biomedical, pharmaceutical, coating, and petroleum industries since they influence (bio)colloidal transport phenomena and nanoparticle stability [1]. From a property measurement point of view, understanding viscoelastic flows induced by a small-amplitude oscillation of a colloidal particle is important for inferring the local microstructure in a suspension through the complex viscosity, typically measured by microrheology using diffusing wave spectroscopy. Microrheology has been widely used to aim at probing the degree of viscous dissipation and stored elastic energy in complex fluids, such as polymer gel and solutions, charged colloidal dispersions, and (bio)soft materials [2–7]. Waigh [8] and Squires and Mason [9], and more recently Zia [10] have provided comprehensive reviews about recent experimental and theoretical advances in microrheology. A broad range of topics on rheology of colloidal suspensions has been compiled and discussed by Mewis and Wagner [11]. A large amount of theoretical analyses, simulations, and experiments [12–28] have addressed linear and nonlinear viscoelasticity and diffusional properties of concentrated colloidal dispersions. The evolution of the pair probability distribution function, and the force and stress of the hard-sphere suspensions were derived, computed, and experimentally observed to infer nonlinear viscoelastic and diffusional properties of the suspensions with shear-dependent nonequilibrium microstructure. Microrheological measurements only require a small

*Corresponding author: thfan@engr.uconn.edu

amount of sample, and the method is capable of probing a broad range of frequency-dependent properties beyond what conventional rheometers can access, which is a great advantage for precision and localized measurements of complex fluids.

In a presumed homogeneous medium at thermal equilibrium, the hydrodynamic mobility, the resistance coefficient, the mechanical response function, and the general or frequency-dependent Stokes-Einstein relationship for a spherical colloidal probe are well established [29]. The Stokes-Einstein relation connects fluid properties, friction constant, mean square displacement, and auto- or cross-correlation functions of the colloidal motion in a homogeneous fluid medium and is used for both active (resistance is measured directly) and passive (based on statistics of Brownian motion) probing techniques. From such measurements on a uniform fluid one can extract rheological properties such as the complex shear viscosity or shear modulus, which is composed of elastic and viscous contributions in the response of the medium. However, if the microenvironment is heterogeneous with respect to the probe size, or the microenvironment is perturbed by the appearance of the colloidal probe, interpretation of experimental data can be challenging. To overcome this difficulty, Crocker *et al.* [30] developed two-point microrheology that relies on the cross-correlated thermal motion that appears to be more sensitive to the fluid medium in between than the autocorrelated motion, which is mostly determined by the local inhomogeneity around the caged colloid. The theoretical bases and methodologies were first provided by Levine and Lubensky [31–33] by approximating the general displacement compliance or response function that couples the permeable and elastic network to a viscous solvent. Chen *et al.* [34] have applied this approximation to estimate the properties of the λ-DNA solution and found a depletion thickness twice as large as the mean-field approximation. A depletion layer appears around a protein when considering the mobility of protein molecules in crowded macromolecular media such as concentrated DNA and/or polysaccharide biopolymers in living cells or many biological systems [35]. To enhance the statistics, an optically clamped two-point measurement was developed by Starrs and Bartlett [36]. They found that the polymer depletion effect on hydrodynamics may significantly change the ratio of auto- and cross-correlated response functions. The microdynamics of stochastic interactions of a pair of Brownian hard spheres in a nonadsorbing polymer solution was simulated by Karzar-Jeddi *et al.* [37] by including a complete pair mobility analysis with the depletion effect. Since an explicit description and characterization of the viscoelastic flow near the polymer depleted region is not available, there is a need to revisit the one- and two-point microrheological models and to quantify the apparent viscoelasticity under various polymer conditions. Such investigations give insights into the influence of the presence of particles to (nonadsorbing) polymer solutions, and on the transport properties of such fluid mixtures.

The polymer depletion effect in colloid-polymer mixtures and the resulting attractive potential between colloidal particles were first understood by Asakura and Oosawa in the 1950s [38,39]. Later investigations were mainly on the phase behavior, depletion forces, and equilibrium properties of colloid-polymer mixtures [40–47], including rod-shaped depletants [48–50]. It is clear that the presence of the depletion layer around a colloidal sphere affects its mobility [51]. The change of diffusivity or Stokes resistance (frictional coefficient) experienced by a Brownian sphere in polymer solutions have been investigated extensively, both experimentally and theoretically; see Refs. [52–67]. However, only few experimental studies have addressed the mediation of polymer depletion on the apparent rheological properties and colloidal motion in non-Newtonian nonadsorbing polymer solutions [36,68–70]. Sellers *et al.* [71] provided an analytical expression of translational oscillatory motion of a sphere within an incompressible and uniform viscoelastic medium. The model also includes the small nonlinear inertial effect. The dynamic response of a polymer depletion layer near a planar and oscillatory interface was investigated by Sozanski *et al.* [72] experimentally by using a quartz tuning fork. The fully coupled convective polymer transport with polymer depletion effect was developed by Taniguchi *et al.* [73] by using the ground-state approximation and dynamic self-consistent field theory for a polymer solution in a slit. As far as we are aware of, theory for the flow induced by an oscillatory sphere in a nonuniform viscoelastic polymer medium has not yet been developed. Here we extend the reduced-order, quasistationary continuum models

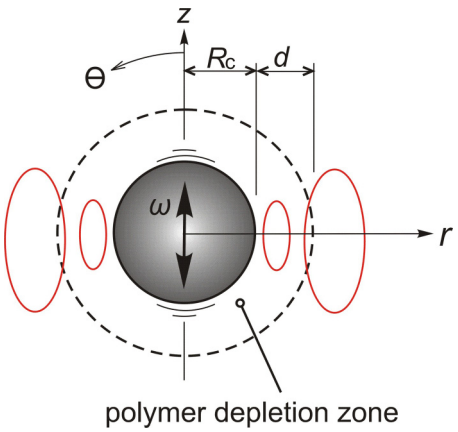

FIG. 1. Polymer depletion zone around a spherical particle undergoing a small amplitude, axisymmetric oscillation along the vertical direction. R_c is particle radius, d is the characteristic depletion thickness, θ is the polar angle, r indicates radial position, z is the symmetry axis along $\theta = 0$, and ω is the oscillation frequency. The three-dimensional toroidal vortices are first introduced at the turns of moving directions and later expand and dissipate into the bulk.

for Newtonian fluids [61,62] to resolve the transient dynamics of linear viscoelastic flow induced by a translationally oscillating sphere in the small amplitude limit. The general Maxwell model is applied to demonstrate the modified complex drag force contributed by the dissipation, added mass, and multiscale polymer relaxation along with the depletion effect.

II. THEORETICAL ANALYSIS

A. Polymer conditions and simplified segment distribution

There exists a wide variety of viscoelastic fluids with different microstructure. To simplify the analysis we limit the scope of this study to a class of fluids that follows single- or multi-mode Maxwell relationships. The apparent values of frequency-dependent properties obtained are compared with the assumed measurable bulk properties. The oscillatory flow pattern is explicitly provided in real space for weakly entangled, dilute-to-semidilute polymer solutions under various solvency conditions. In the dilute-to-semidilute regime of interest, e.g., polymer segment volume fraction $\phi \lesssim \phi^* \ll 1$, where ϕ^* is the polymer overlap concentration, above which polymer coils overlap significantly. Within this regime, the complex viscosity increases gradually as the concentration increases, and the bulk solution is assumed to be a uniform viscoelastic fluid.

The characteristic length of the flow induced by the colloidal probe is defined by the colloid radius R_c (see Fig. 1), and we consider cases of linear polymer chains with radius of gyration R_g larger than or about the order of the polymer correlation length ξ, i.e., $a \ll \xi \lesssim R_g \lesssim R_c$, where a is the effective polymer segment length. The equilibrium polymer depletion thickness can be characterized by a range in between the radius of gyration in the limit of infinite dilution and the correlation length [45], depending on solvency and the bulk polymer concentration. During fluid motion, the polymer-solvent interfacial friction coefficient ζ is a local quantity and is related to the polymer correlation length ξ, segment or persistence length a, solvency scaling exponent m ($m = 1$ for a Θ solvent and $m = 3/4$ for a good solvent), solvent viscosity η_s, and the volume fraction of polymer segments ϕ [74], expressed as

$$\zeta(\phi) \simeq \frac{6\pi\eta_s}{\xi^2} = \frac{6\pi\eta_s}{a^2}\phi^{2m}, \tag{1}$$

where $\xi(\phi) \simeq a\phi^{-m}$. The elasticity at the probing timescale is assumed due to the weak entanglement between polymer chains or relaxation of their internal configuration. A linear polymer with an assumed segment length $a \simeq 0.40$ to 4.0 nm and a radius of gyration $R_g \simeq 50$ to 500 nm is selected for the case study. Considering a and R_g as input parameters, and $R_g \simeq a(N/6)^{\nu}$, where the Flory exponent $\nu = 3/5$ for a good solvent and $\nu = 1/2$ for a Θ solvent, and the estimated degree of polymerization $N = 93\,750 \gg 1$ and as an ideal chain. The polymer segment volume fraction at overlap is therefore

$$\phi^* \simeq \frac{3}{4\pi}(6)^{3\nu}N^{1-3\nu} \simeq 0.000\,63 \left(\text{for } \nu = \frac{3}{5}\right) \text{ to } 0.011 \left(\nu = \frac{1}{2}\right) \ll 1.$$

In our studies the bulk polymer concentration is assumed up to about $3\phi^*$ in the semidilute regime. Considering ϕ^* as a characteristic volume fraction, the corresponding polymer correlation length is $\xi(\phi) \sim a\phi^{-m} \simeq 100$ to 1000 nm for a good solvent with solvency factor $m = 3/4$ and $a \simeq 0.4$ to 4 nm, and $\xi(\phi) \simeq 34.9$ and 349 nm for a Θ solvent with $m = 1$. Note that $(3\nu - 1)(3m - 1) = 1$. As a result, the polymer blob diffusion time τ_ξ, which indicates the relaxation of the blob distribution around the colloids due to thermal fluctuation, can be estimated by using the polymer correlation length and the blob diffusivity as

$$\tau_\xi \sim \frac{\xi^2}{D_{\text{blob}}} \sim \frac{a^2(\phi^*)^{-2m}}{(\phi^*)^{1-2m}D_{\text{seg}}} \sim \frac{6\pi\eta_s a^3}{\phi^* kT} \simeq 2.6 \times 10^{-8} \text{ to } 4.7 \times 10^{-4} \text{ s}$$

for both segment lengths under Θ solvents or good solvents, where D_{seg} is the segment diffusivity. This timescale is considered to be equal to fundamental relaxation time λ_1.

For $\omega \simeq 1$ to 10^5 s^{-1}, the shear effect induced by the oscillatory motion on the distribution of polymers can be estimated by the Péclet number as

$$\mathcal{P}_e = \tau_\xi \omega \simeq 10^{-8} \text{ to } 10.$$

As a first approximation at a relatively low Péclet-number regime, we assume that the small-amplitude oscillation is within the depletion zone such that the distortion of the depletion layer due to transient and convective effects is negligible. This implies that the depletion zone surrounding the sphere does not deform and the distribution of nonadsorbing polymers is approximately at equilibrium. The flow dynamics is periodic while the local viscosity and polymer concentration are quasistationary. Although the Reynolds number is small and the nonlinear inertial effect for the fluid motion is negligible, the local acceleration of the fluid motion is significant in the oscillatory motion. Here we simplify the problem by considering a monochromatic, small-amplitude (smaller than the apparent depletion thickness), translational, oscillatory motion of a colloidal sphere in an otherwise quiescent polymer fluid (Fig. 1). We first present a simplified two-layer analytical result and then a numerical model that incorporates a continuous polymer concentration profile based on the mean-field approximation for polymer solutions. Both single mode and multimode Maxwell models are demonstrated for extracting the apparent complex viscosity. In summary, modeling of the oscillatory colloidal probe in a polymer solution is determined by the following key parameters: (i) solvent condition described by the Flory exponent υ and solvency factor m, Huggins coefficient k_H, thermal energy kT at the assumed ambient temperature, and the solvent viscosity η_s; (ii) size parameters including the probe radius R_c, polymer segment length a, polymer radius of gyration R_g, and the degree of polymerization N; (iii) polymer bulk concentration ϕ_b and the overlap fraction ϕ^*; and (iv) probe oscillating frequency ω and an amplitude much smaller than the apparent depletion thickness d.

B. Two-layer approximation

In the simplified two-layer approximation, the small-amplitude oscillatory flow in a linear, incompressible, viscoelastic continuum can be described by the momentum equations:

$$\rho^{(\mathrm{i})}\frac{\partial \boldsymbol{v}^{(\mathrm{i})}(r,\theta,t)}{\partial t} \simeq -\nabla p^{(\mathrm{i})}(r,\theta,t) + \eta^{*(\mathrm{i})}(\omega)\nabla^2 \boldsymbol{v}^{(\mathrm{i})}, \tag{2}$$

for $R_c \leqslant r \leqslant R_c + d$, and

$$\rho^{(\mathrm{o})}\frac{\partial \boldsymbol{v}^{(\mathrm{o})}(r,\theta,t)}{\partial t} \simeq -\nabla p^{(\mathrm{o})}(r,\theta,t) + \eta^{*(\mathrm{o})}(\omega)\nabla^2 \boldsymbol{v}^{(\mathrm{o})}, \tag{3}$$

for $R_c + d \leqslant r < \infty$, where $\boldsymbol{v}^{(\mathrm{i})}$, $p^{(\mathrm{i})}$, $\boldsymbol{v}^{(\mathrm{o})}$, and $p^{(\mathrm{o})}$ are the complex velocity and pressure fields in the inner and outer domains, denoted by (i) and (o), respectively, t is time, ω is the circular frequency of the oscillation, η^* is the complex viscosity, R_c is the colloidal radius, r is the radial coordinate, and d is the mean-field approximation of the depletion thickness based on polymer chain length, correlation length, solvency and bulk polymer concentration [45]. The complex viscosity is introduced to model the Maxwell viscoelastic fluid. The inner layer fluid density is approximately the same as the outer layer, i.e., $\rho^{(\mathrm{i})} \simeq \rho^{(\mathrm{o})} = \rho$. The incompressible continuity equations are

$$\nabla \cdot \boldsymbol{v}^{(\mathrm{i})} = 0 \quad \text{and} \quad \nabla \cdot \boldsymbol{v}^{(\mathrm{o})} = 0, \tag{4}$$

respectively.

The velocity boundary condition on the sphere is

$$\boldsymbol{v}^{(\mathrm{i})} = U e^{i\omega t}\hat{\mathbf{e}}_{\mathrm{z}} \quad \text{at } r = R_c, \tag{5}$$

where U is the real velocity amplitude of the oscillatory sphere, $\hat{\mathbf{e}}_{\mathrm{z}}$ is the unit vector along the axis of symmetry. The velocity and pressure conditions at the far field are

$$p \to p_\infty \quad \text{and} \quad \boldsymbol{v} \to 0 \quad \text{as } r \to \infty. \tag{6}$$

At the interface between both domains we assume that there exists no interfacial energy and the velocity and stress fields are continuous, written as

$$\boldsymbol{v}^{(\mathrm{i})} = \boldsymbol{v}^{(\mathrm{o})} \quad \text{and} \quad \boldsymbol{\tau}^{(\mathrm{i})} = \boldsymbol{\tau}^{(\mathrm{o})} \quad \text{at } r = R_c + d. \tag{7}$$

Hereafter $\boldsymbol{\tau}$ indicates the stress field including the pressure contribution, and $\boldsymbol{\sigma}$ denotes the deviatoric part of the stress.

The complex viscosity for the generalized Maxwell model [75,76] can be expressed as

$$\eta^* = \eta' - i\eta'' = \sum_{j=1}^{n}\frac{\eta_j}{1+\omega^2\lambda_j^2} - i\sum_{j=1}^{n}\frac{\eta_j\omega\lambda_j}{1+\omega^2\lambda_j^2}, \tag{8}$$

where $\lambda_1 > \lambda_2 > \cdots > \lambda_n$ represents the spectrum of discrete relaxation times for the complex medium fluid, n is the number of modes, and η_j is the discrete viscosity corresponding to relaxation mode i, which may be reduced to the following format:

$$\eta_j = \eta_0\frac{\lambda_j}{\sum_j \lambda_j} \quad \text{and} \quad \lambda_j = \frac{\lambda_1}{j^q}, \tag{9}$$

where η_0 is the zero-frequency (zero-shear) viscosity of the polymer solution, λ_1 is the largest relaxation time, and $q \simeq 2$ for the Rouse model [75,77]. In the two-layer approximation, we approximate the local value of η_0 within and outside the depletion zone by using a step function:

$$\eta_0(r) = \begin{cases} \eta_s \text{ or } \eta_0^{(\mathrm{i})} & \text{for } R_c \leqslant r \leqslant R_c + d \\ \eta_0^{(\mathrm{o})} & \text{for } R_c + d \leqslant r < \infty, \end{cases} \tag{10}$$

where the subscript 0 indicates the Newtonian or zero-frequency limit, superscripts (i) and (o) represent the inner and outer layers, respectively, $\eta_0^{(\mathrm{i})}$ is essentially the solvent viscosity η_s, while $\eta_0^{(\mathrm{o})}$ represents the bulk viscoelastic fluid outside the depletion layer. The corresponding polymer mass concentration is $c(r) = 0$ in the inner layer, and $c(r) = c_b$ as the bulk polymer concentration for the outer domain. Here the single-mode Maxwell model is applied to the two-layer analytical approximation, while both single- and multiscale Maxwell models are applied for the numerical approach with a continuous distribution of polymer segment concentration.

Considering the oscillatory fluid motion with the same frequency as the moving sphere, the characteristic scales for the length, time, velocity, complex viscosity, stress and pressure, and drag force can be selected and expressed as

$$r \sim R_c, \quad t \sim 1/\omega, \quad \boldsymbol{v} \sim U, \quad \eta^* \sim \eta_s, \tag{11}$$

and

$$\boldsymbol{\tau} \text{ and } p \sim \eta_s U/R_c, \quad \text{Drag } \mathcal{F} \sim 6\pi\eta_s R_c U, \tag{12}$$

where the total force is scaled by the steady Stokes drag in solvent. Hereafter formulations are in dimensionless form unless further notification. By substituting the location- and time-dependent periodic velocity and pressure fields, i.e.,

$$[\boldsymbol{v}^{(\mathrm{i})}(r,\theta,t),\ \boldsymbol{v}^{(\mathrm{o})}(r,\theta,t)] = [\tilde{\boldsymbol{v}}^{(\mathrm{i})}(r,\theta),\ \tilde{\boldsymbol{v}}^{(\mathrm{o})}(r,\theta)]e^{it}, \tag{13}$$

and

$$[p^{(\mathrm{i})}(r,\theta,t),\ p^{(\mathrm{o})}(r,\theta,t)] = [\tilde{p}^{(\mathrm{i})}(r,\theta),\ \tilde{p}^{(\mathrm{o})}(r,\theta)]e^{it} + [p_\infty,\ p_\infty], \tag{14}$$

into the momentum equations, with the tilde on variables indicating the complex amplitudes of the transient fields, and in terms of the scaled variables, we obtain

$$i\beta\tilde{\boldsymbol{v}}^{(\mathrm{i})} = -\nabla\tilde{p}^{(\mathrm{i})} + \overline{\eta}^*\nabla^2\tilde{\boldsymbol{v}}^{(\mathrm{i})}, \tag{15}$$

for $1 \leqslant r \leqslant 1 + d$, and

$$i\beta\tilde{\boldsymbol{v}}^{(\mathrm{o})} = -\nabla\tilde{p}^{(\mathrm{o})} + \alpha_b\overline{\eta}^*\nabla^2\tilde{\boldsymbol{v}}^{(\mathrm{o})}, \tag{16}$$

for $1 + d \leqslant r < \infty$, where d here is the dimensionless depletion thickness. The three characteristic numbers are defined as

$$\alpha_b = \frac{\eta_0^{(\mathrm{o})}}{\eta_s}, \quad \beta = \frac{\rho\omega R_c^2}{\eta_s}, \quad \mathrm{De} = \lambda\omega, \tag{17}$$

and the single-mode complex viscosity can be written as

$$\frac{\eta^*}{\eta_s} = \alpha_b\,\overline{\eta}^*, \quad \text{where } \overline{\eta}^*(\mathrm{De}) = \frac{1 - i\mathrm{De}}{1 + \mathrm{De}^2}. \tag{18}$$

Here α_b is the dimensionless, zero-shear, bulk-to-solvent viscosity ratio for the two-layer model, the frequency parameter β determines the degree of local acceleration, and the Deborah number De is the ratio of material stress relaxation (λ) to the active oscillation ($1/\omega$) timescales, or the scaled material relaxation time. Both β and De are proportional to the driving frequency ω. The material expresses fluid-like behavior at small De.

At least two approaches can be applied to resolve the transient Stokes flow problems in hand: the pseudovector [78,79] and the stream function method [80,81]. Here we follow the pseudovector methodology for its concise algebraic operation by representing the complex velocity amplitudes in terms of radially dependent functions $f^{(\mathrm{i})}$ and $f^{(\mathrm{o})}$, expressed as

$$\tilde{\boldsymbol{v}}^{(\mathrm{i})} = \nabla \times [\nabla f^{(\mathrm{i})} \times \hat{\mathbf{e}}_z] = \nabla \times \nabla \times (f^{(\mathrm{i})}\hat{\mathbf{e}}_z), \tag{19}$$

$$\tilde{\boldsymbol{v}}^{(\mathrm{o})} = \nabla \times [\nabla f^{(\mathrm{o})} \times \hat{\mathbf{e}}_z] = \nabla \times \nabla \times (f^{(\mathrm{o})}\hat{\mathbf{e}}_z), \tag{20}$$

where the terms within the brackets are arbitrary pseudovectors so that the velocity satisfies the continuity equation. Only the first- and second-order derivatives of the function f are needed for solving this problem. By taking the curl of both momentum equations (15) and (16) to eliminate pressure terms and substituting the above expressions, the momentum equations reduce to

$$\nabla^2\nabla^2\boldsymbol{\nabla} f^{(\mathrm{i})} - \frac{i\beta}{\overline{\eta}^*}\nabla^2\boldsymbol{\nabla} f^{(\mathrm{i})} = 0, \tag{21}$$

and

$$\nabla^2\nabla^2\boldsymbol{\nabla} f^{(\mathrm{o})} - \frac{i\beta}{\alpha_b\overline{\eta}^*}\nabla^2\boldsymbol{\nabla} f^{(\mathrm{o})} = 0, \tag{22}$$

for the corresponding inner and outer domains. Integrating above momentum equations once, we obtain

$$\nabla^2\nabla^2 f^{(\mathrm{i})} + {k^{(\mathrm{i})}}^2\nabla^2 f^{(\mathrm{i})} = A, \tag{23}$$

$$\nabla^2\nabla^2 f^{(\mathrm{o})} + {k^{(\mathrm{o})}}^2\nabla^2 f^{(\mathrm{o})} = B, \tag{24}$$

respectively, where the constant A is to be determined by matching the interfacial boundary conditions between the inner and outer domains, and the constant B vanishes in the outer domain due to the quiescent far-field velocity boundary condition determined by the derivatives of the f function. The characteristic inner and outer complex wave numbers are associated with the complex viscosity as

$$k^{(\mathrm{i})} = (i-1)\sqrt{\frac{\beta}{2\overline{\eta}^*}} = \frac{i-1}{\delta^{(\mathrm{i})}}, \tag{25}$$

$$k^{(\mathrm{o})} = (i-1)\sqrt{\frac{\beta}{2\alpha_b\overline{\eta}^*}} = \frac{i-1}{\delta^{(\mathrm{o})}}, \tag{26}$$

where the resulting $\delta^{(\mathrm{i})}$ and $\delta^{(\mathrm{o})}$ are characteristic penetration depths of the decayed viscous wave in each domain. The factor 2 inside the square roots in equations (25) and (26) comes from $\sqrt{-i} = (1-i)/\sqrt{2}$, and the sign for the wave vector k is determined in a way that the velocity field shows an exponential decay with radial distance r, and the derivatives of the function f vanishes at far field. The intermediate general solutions of Eqs. (23) and (24) in terms of the second-order derivatives are

$$\nabla^2 f^{(\mathrm{i})} = \frac{C_1 e^{ik^{(\mathrm{i})}r}}{r} + \frac{C_2 e^{-ik^{(\mathrm{i})}r}}{r} + \frac{A}{{k^{(\mathrm{i})}}^2}, \tag{27}$$

$$\nabla^2 f^{(\mathrm{o})} = \frac{D_1 e^{ik^{(\mathrm{o})}r}}{r}. \tag{28}$$

Note that the growing term vanishes for the outer domain due to the far-field boundary condition. Integrating Eqs. (27) and (28) once and combining unknown coefficients, we obtain the general solutions of the first-order derivatives of both f functions:

$$\frac{df^{(\mathrm{i})}}{dr} = \frac{A}{3{k^{(\mathrm{i})}}^2}r + \frac{1}{r^2}\left[a^{(\mathrm{i})}e^{ik^{(\mathrm{i})}r}\left(r - \frac{1}{ik^{(\mathrm{i})}}\right)\right] + \frac{b^{(\mathrm{i})}}{r^2} + \frac{1}{r^2}\left[c^{(\mathrm{i})}e^{-ik^{(\mathrm{i})}r}\left(r + \frac{1}{ik^{(\mathrm{i})}}\right)\right], \tag{29}$$

$$\frac{df^{(\mathrm{o})}}{dr} = \frac{1}{r^2}\left[a^{(\mathrm{o})}e^{ik^{(\mathrm{o})}r}\left(r - \frac{1}{ik^{(\mathrm{o})}}\right)\right] + \frac{b^{(\mathrm{o})}}{r^2}, \tag{30}$$

respectively, where $a^{(\mathrm{i})} = C_1/ik^{(\mathrm{i})}$, $c^{(\mathrm{i})} = C_2/ik^{(\mathrm{i})}$, $a^{(\mathrm{o})} = D_1/ik^{(\mathrm{i})}$. Only the derivatives instead of the actual forms of the f functions are used in solving the velocity field. The six unknown coefficients

A, $a^{(\mathrm{i})}$, $b^{(\mathrm{i})}$, $c^{(\mathrm{i})}$, $a^{(\mathrm{o})}$, and $b^{(\mathrm{o})}$ are to be determined by the no-slip boundary condition on the particle surface, and continuous velocity and stress conditions across the interface of the depletion zone:

$$\tilde{v}_r^{(\mathrm{i})} = \cos\theta, \quad \tilde{v}_\theta^{(\mathrm{i})} = -\sin\theta \quad \text{at } r = 1, \tag{31a}$$

$$\tilde{v}_r^{(\mathrm{i})} = \tilde{v}_r^{(\mathrm{o})}, \quad \tilde{v}_\theta^{(\mathrm{i})} = \tilde{v}_\theta^{(\mathrm{o})} \quad \text{at } r = 1 + d, \tag{31b}$$

$$\tilde{\sigma}_{r\theta}^{(\mathrm{i})} = \tilde{\sigma}_{r\theta}^{(\mathrm{o})} \quad \text{at } r = 1 + d, \tag{31c}$$

$$-\tilde{p}^{(\mathrm{i})} + \tilde{\sigma}_{rr}^{(\mathrm{i})} = -\tilde{p}^{(\mathrm{o})} + \tilde{\sigma}_{rr}^{(\mathrm{o})} \quad \text{at } r = 1 + d. \tag{31d}$$

Note that the far-field velocity and stress vanish as $r \to \infty$, and the polymer-induced osmotic pressure in the outer fluid has been included in $\tilde{p}^{(\mathrm{o})}$ as a modified pressure. The six coefficients can be determined by substituting the f derivatives into Eqs. (19) and (20) and then into the velocity and stress boundary conditions. The pressure field is determined by integrating the momentum equation directly. The lengthy derivation can be simplified by applying the vector identity

$$\boldsymbol{\nabla} \times \boldsymbol{\nabla} \times (f\hat{\mathbf{e}}_z) \equiv \boldsymbol{\nabla}(\boldsymbol{\nabla} \cdot f\hat{\mathbf{e}}_z) - \nabla^2(f\hat{\mathbf{e}}_z) \tag{32}$$

into the algebraic operations. In summary, the resulting analytical solution for the six unknown coefficients can be obtained and presented by the following matrix form:

$$\begin{bmatrix} A \\ a^{(\mathrm{i})} \\ b^{(\mathrm{i})} \\ c^{(\mathrm{i})} \\ a^{(\mathrm{o})} \\ b^{(\mathrm{o})} \end{bmatrix} = \begin{bmatrix} -2/3k^{(\mathrm{i})2} & B(k^{(\mathrm{i})}, 1) & -2 & C(k^{(\mathrm{i})}, 1) & 0 & 0 \\ -2/3k^{(\mathrm{i})2} & D(k^{(\mathrm{i})}, 1) & 1 & E(k^{(\mathrm{i})}, 1) & 0 & 0 \\ -2/3k^{(\mathrm{i})2} & B(k^{(\mathrm{i})}, d_\mathrm{s}) & -2/d_\mathrm{s}^3 & C(k^{(\mathrm{i})}, d_\mathrm{s}) & -B(k^{(\mathrm{o})}, d_\mathrm{s}) & 2/d_\mathrm{s}^3 \\ -2/3k^{(\mathrm{i})2} & D(k^{(\mathrm{i})}, d_\mathrm{s}) & 1/d_\mathrm{s}^3 & E(k^{(\mathrm{i})}, d_\mathrm{s}) & -D(k^{(\mathrm{o})}, d_\mathrm{s}) & -1/d_\mathrm{s}^3 \\ 2d_\mathrm{s}/3 & 2F(k^{(\mathrm{i})}, d_\mathrm{s}) & (12/d_\mathrm{s}^4) - (k^{(\mathrm{i})}/d_\mathrm{s})^2 & 2G(k^{(\mathrm{i})}, d_\mathrm{s}) & -2\alpha_b F(k^{(\mathrm{o})}, d_\mathrm{s}) & \alpha_b\left(k^{(\mathrm{o})2}/d_\mathrm{s}^2 - 12/d_s^4\right) \\ 0 & H(k^{(\mathrm{i})}, d_\mathrm{s}) & -6/d_\mathrm{s}^4 & I(k^{(\mathrm{i})}, d_\mathrm{s}) & -\alpha_b H(k^{(\mathrm{o})}, d_\mathrm{s}) & 6\alpha_b/d_\mathrm{s}^4 \end{bmatrix}^{-1} \times \begin{bmatrix} 1 \\ 1 \\ 0 \\ 0 \\ 0 \\ 0 \end{bmatrix}, \tag{33}$$

where $d_\mathrm{s} = 1 + d$, and

$$B(k,r) = e^{ikr}\left(\frac{-2}{r^2} + \frac{2}{ikr^3}\right), \quad C(k,r) = e^{-ikr}\left(\frac{-2}{r^2} - \frac{2}{ikr^3}\right),$$

$$D(k,r) = e^{ikr}\left(\frac{1}{r^2} - \frac{1}{ikr^3} - \frac{ik}{r}\right), \quad E(k,r) = e^{-ikr}\left(\frac{1}{r^2} + \frac{1}{ikr^3} + \frac{ik}{r}\right),$$

$$F(k,r) = e^{ikr}\left(\frac{-6}{ikr^4} + \frac{6}{r^3} - \frac{2ik}{r^2}\right), \quad G(k,r) = e^{-ikr}\left(\frac{6}{ikr^4} + \frac{6}{r^3} + \frac{2ik}{r^2}\right),$$

$$H(k,r) = e^{ikr}\left(\frac{6}{ikr^4} - \frac{6}{r^3} + \frac{3ik}{r^2} + \frac{k^2}{r}\right), \quad I(k,r) = e^{-ikr}\left(\frac{-6}{ikr^4} - \frac{6}{r^3} - \frac{3ik}{r^2} + \frac{k^2}{r}\right). \tag{34}$$

Finally, the resulting complex amplitudes of the velocity field can be expressed as

$$\tilde{v}_r^{(\mathrm{i})} = \cos\theta\left[\frac{-2A}{3k^{(\mathrm{i})2}} + a^{(\mathrm{i})}B(k^{(\mathrm{i})}, r) - \frac{2b^{(\mathrm{i})}}{r^3} + c^{(\mathrm{i})}C(k^{(\mathrm{i})}, r)\right], \tag{35a}$$

$$\tilde{v}_\theta^{(\mathrm{i})} = -\sin\theta\left[\frac{-2A}{3k^{(\mathrm{i})2}} + a^{(\mathrm{i})}D(k^{(\mathrm{i})}, r) + \frac{b^{(\mathrm{i})}}{r^3} + c^{(\mathrm{i})}E(k^{(\mathrm{i})}, r)\right], \tag{35b}$$

$$\tilde{v}_r^{(\mathrm{o})} = \cos\theta\left[a^{(\mathrm{o})}B(k^{(\mathrm{o})}, r) - \frac{2b^{(\mathrm{o})}}{r^3}\right], \tag{35c}$$

$$\tilde{v}_\theta^{(\mathrm{o})} = -\sin\theta\left[a^{(\mathrm{o})}D(k^{(\mathrm{o})}, r) + \frac{b^{(\mathrm{o})}}{r^3}\right], \tag{35d}$$

and therefore the deviatoric stress amplitudes in both domains are

$$\tilde{\sigma}_{rr}^{(\mathrm{i})} = 2\overline{\eta}^*\cos\theta\left[a^{(\mathrm{i})}F(k^{(\mathrm{i})}, r) + \frac{6b^{(\mathrm{i})}}{r^4} + c^{(\mathrm{i})}G(k^{(\mathrm{i})}, r)\right], \tag{36a}$$

$$\tilde{\sigma}_{rr}^{(\mathrm{o})} = 2\alpha_b\overline{\eta}^*\cos\theta\left[a^{(\mathrm{o})}F(k^{(\mathrm{o})}, r) + \frac{6b^{(\mathrm{o})}}{r^4}\right], \tag{36b}$$

$$\tilde{\sigma}_{r\theta}^{(\mathrm{i})} = -\overline{\eta}^*\sin\theta\left[a^{(\mathrm{i})}H(k^{(\mathrm{i})}, r) - \frac{6b^{(\mathrm{i})}}{r^4} + c^{(\mathrm{i})}I(k^{(\mathrm{i})}, r)\right], \tag{36c}$$

$$\tilde{\sigma}_{r\theta}^{(\mathrm{o})} = -\alpha_b\,\overline{\eta}^*\sin\theta\left[a^{(\mathrm{o})}H(k^{(\mathrm{o})}, r) - \frac{6b^{(\mathrm{o})}}{r^4}\right]. \tag{36d}$$

From momentum equations (15) and (16), both pressure amplitudes can be obtained and expressed as

$$\tilde{p}^{(\mathrm{i})} = \overline{\eta}^*\cos\theta\left[-\frac{2A}{3}r + \frac{k^{(\mathrm{i})2}b^{(\mathrm{i})}}{r^2}\right], \tag{37a}$$

$$\tilde{p}^{(\mathrm{o})} = \alpha_b\,\overline{\eta}^*\cos\theta\left[\frac{k^{(\mathrm{o})2}b^{(\mathrm{o})}}{r^2}\right]. \tag{37b}$$

Finally from the area integration of the surface stress, we obtain the overall hydrodynamic drag acting on the sphere, $\mathcal{F} = \tilde{\mathcal{F}}e^{it}$, where the complex amplitude is

$$\tilde{\mathcal{F}}_{2\mathrm{M}}(\alpha_b, \beta, \mathrm{De}, d) = -\overline{\eta}^*\left\{\frac{2}{9}\left[-\frac{2}{3}A + k^{(\mathrm{i})2}b^{(\mathrm{i})}\right] - \frac{4}{9}[a^{(\mathrm{i})}H(k^{(\mathrm{i})}, 1) - 6b^{(\mathrm{i})} + c^{(\mathrm{i})}I(k^{(\mathrm{i})}, 1)]\right\}, \tag{38}$$

where the subscript 2M indicates the two-layer Maxwell model.

C. Numerical validation using continuous concentration profile

The apparent depletion thickness based on the mean-field approximation is roughly the polymer radius of gyration in dilute polymer solutions and the polymer correlation length in semidilute solutions [45]. The two-layer model can better describe the Stokes drag for cases with relatively thin depletion layer thickness as compared with the particle radius [62]. Similarly, the two-layer viscoelastic model and its applicability can be validated numerically by using a continuous and spherically symmetric polymer concentration profile, schematically shown in Fig. 2(a). Figure 2(b) demonstrates the corresponding zero-shear viscosity. First, the dimensional momentum equation for a nonuniform linear viscoelastic fluid can be expressed as

$$\rho\frac{\partial \boldsymbol{v}}{\partial t} \simeq -\nabla p + \nabla\cdot\{\eta^*[\nabla\boldsymbol{v} + (\nabla\boldsymbol{v})^T]\}, \tag{39}$$

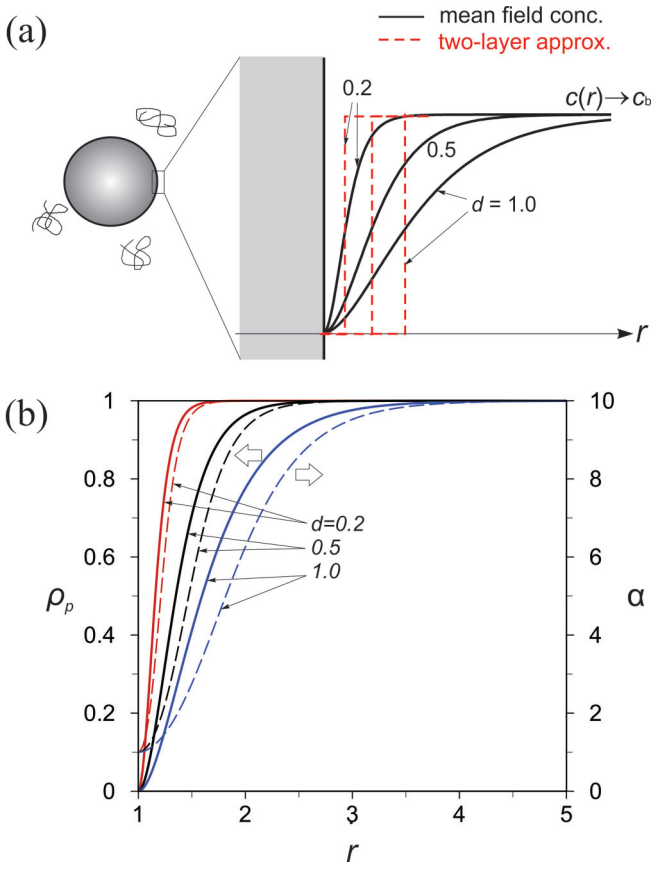

FIG. 2. (a) A schematic showing the equilibrium polymer concentration profiles with various characteristic depletion thickness d, and their corresponding two-layer approximations. (b) The scaled zero-shear viscosity with respect to polymer local concentration for the case with bulk viscosity about ten times of the solvent viscosity ($[\eta]c_b \simeq 2.534$).

where ρ is fluid density, η^* here represents complex viscosity as a continuous function of local polymer concentration, which gradually increases from the surface to the bulk. In terms of the characteristic depletion thickness d [74], the mean-field approximation of the concentration for a spherical surface [45,82] gives

$$\rho_{\mathrm{p}}(r) = \frac{c(r)}{c_{\mathrm{b}}} \simeq \left[r - 1 + \tanh\left(\frac{r-1}{d} \right) \right]^2 \Big/ r^2 \tag{40}$$

for $1 \leqslant r < \infty$, which represents the ratio of local-to-bulk polymer concentration. Here we assume that the local zero-frequency viscosity $\eta_0(r)$, which appeared in Eq. (8), connects the scaled polymer concentration $\rho_{\mathrm{p}}(r)$ through the Martin's equation [83,84], expressed as an exponential function as

$$\alpha(r) = \frac{\eta_0(r)}{\eta_s} = 1 + [\eta]c_{\mathrm{b}}\rho_{\mathrm{p}}(r)e^{k_H[\eta]c_{\mathrm{b}}\rho_{\mathrm{p}}(r)}, \tag{41}$$

where k_H is the Huggins coefficient (assumed 0.5 for all test cases in this study as a value close to what is found from rheology studies of polymer solutions), $[\eta]$ is the intrinsic viscosity of polymer solutions, and $[\eta]c_b = \phi/\phi_b^*$ represents the scaled local polymer concentration. Following Eqs. (8)

and (9), the scaled complex viscosity therefore can be written as

$$\frac{\eta^*}{\eta_s} = \alpha(r)\overline{\eta}^*(\mathrm{De}), \tag{42}$$

where α gives the local effect to the zero-shear viscosity, and the contribution of the multimode effect is expressed as

$$\overline{\eta}^*(\mathrm{De}) = \frac{1 - i\mathrm{De}}{1 + \mathrm{De}^2} + \frac{1 - i2^{-q}\mathrm{De}}{(1 + 2^q)(1 + 2^{-2q}\mathrm{De}^2)} + \frac{2^q - i2^q 3^{-q}\mathrm{De}}{(6^q + 3^q + 2^q)(1 + 3^{-2q}\mathrm{De}^2)} + \cdots, \tag{43}$$

where the Deborah number $\mathrm{De} = \lambda_1\omega$ corresponds to the slowest relaxation time λ_1.

Similar to the two-layer model we apply the characteristic scales in Eqs. (11) and (12) and consider the following periodic velocity and pressure fields:

$$[\boldsymbol{v}(r,\theta,t),\ p(r,\theta,t)] = [\tilde{\boldsymbol{v}}(r,\theta),\ \tilde{p}(r,\theta)]e^{it} + [0,\ p_\infty]. \tag{44}$$

Substituting the velocity and pressure into the scaled momentum equation, and then combining it with the local complex viscosity we obtain the reduced form:

$$i\beta\tilde{\boldsymbol{v}} = -\boldsymbol{\nabla}\tilde{p} + \overline{\eta}^*\boldsymbol{\nabla}\cdot\{\alpha(r)[\boldsymbol{\nabla}\tilde{\boldsymbol{v}} + (\boldsymbol{\nabla}\tilde{\boldsymbol{v}})^T]\}. \tag{45}$$

The pressure term can be eliminated by taking the curl of the momentum equation. Considering the axisymmetric flow, the velocity amplitude can be further represented by the Stokes stream function $\tilde{\psi}(r,\theta)$ as

$$\tilde{v}_r = \frac{-1}{r^2\sin\theta}\frac{\partial\tilde{\psi}}{\partial\theta}, \quad \tilde{v}_\theta = \frac{1}{r\sin\theta}\frac{\partial\tilde{\psi}}{\partial r}. \tag{46}$$

By applying the following identity to the curl of the Laplacian term in equation (45),

$$-\boldsymbol{\nabla}\times\boldsymbol{\nabla}\times\boldsymbol{\nabla}\times\tilde{\boldsymbol{v}} = \hat{\mathbf{e}}_\varphi\frac{1}{r\sin\theta}(E^4\tilde{\psi}), \tag{47}$$

where the differential operator

$$E^4 \equiv \left[\frac{\partial^2}{\partial r^2} + \frac{\sin\theta}{r^2}\frac{\partial}{\partial\theta}\left(\frac{1}{\sin\theta}\frac{\partial}{\partial\theta}\right)\right]^2,$$

and the trial solution $\tilde{\psi}(r,\theta) = f(r)\sin^2\theta$ to satisfy the complex velocity boundary conditions, $\tilde{v}_r = \cos\theta$, $\tilde{v}_\theta = -\sin\theta$ at $r = 1$, the momentum equation reduces to a fourth-order differential equation for the unknown radial complex function $f(r)$:

$$f^{(4)} + \frac{2\alpha'}{\alpha}f''' - \left[\frac{4}{r^2} + \frac{2\alpha'}{r\alpha} - \frac{\alpha''}{\alpha} + \frac{i\beta}{\alpha\overline{\eta}^*}\right]f'' + \left(\frac{8}{r^3} - \frac{2\alpha'}{r^2\alpha} - \frac{2\alpha''}{r\alpha}\right)f' - \left[\frac{8}{r^4} - \frac{8\alpha'}{r^3\alpha} - \frac{2\alpha''}{r^2\alpha} - \frac{2\beta i}{r^2\alpha\overline{\eta}^*}\right]f = 0 \tag{48}$$

for $1 \leqslant r < \infty$. The corresponding velocity boundary conditions are

$$f(1) = -1/2, \tag{49}$$

$$f'(1) = -1, \tag{50}$$

and

$$\frac{f}{r^2} \to 0 \quad \text{and} \quad \frac{f'}{r} \to 0 \quad \text{as } r \to \infty. \tag{51}$$

The fourth-order equation (48) can then be solved by combining the Runge-Kutta integration and the shooting algorithms to obtain the unknown surface boundary conditions f'' and f''' at $r = 1$

based on the vanishing far-field conditions. The corresponding stress and pressure amplitudes can then be derived from the obtained velocity field. The amplitude of the normal stress is

$$\tilde{\sigma}_{rr} = -4\alpha(r)\overline{\eta}^* \cos\theta\left[\frac{f'}{r^2} - \frac{2f}{r^3}\right], \tag{52}$$

which vanishes at the particle surface. The shear stress amplitude is

$$\tilde{\sigma}_{r\theta} = \alpha(r)\overline{\eta}^* \sin\theta\left[\frac{f''}{r} - \frac{2f'}{r^2} + \frac{2f}{r^3}\right]. \tag{53}$$

The pressure amplitude is

$$\tilde{p} = (i\beta\cos\theta)f' - \overline{\eta}^*\cos\theta\left[\alpha f''' + \alpha' f'' - \left(\frac{2\alpha}{r^2} + \frac{2\alpha'}{r}\right)f' + \left(\frac{4\alpha}{r^3} + \frac{2\alpha'}{r^2}\right)f\right]. \tag{54}$$

Finally, the resulting surface integration of the local stress leads to total drag force amplitude:

$$\tilde{\mathcal{F}}_{\mathrm{cM}} = -\overline{\eta}^*\left[\frac{4}{9} + \frac{4}{9}f''(1) - \frac{2}{9}f'''(1)\right] + \frac{2}{9}i\beta, \tag{55}$$

with $\alpha(1) = 1$ and $\alpha'(1) = 0$. The subscript cM indicates the Maxwell model with continuous concentration profile. The first part accounts for complex viscous effect, whereas the last term contributes to the imaginary part of the force amplitude due to pressure distribution introduced by the transient inertial (added mass) effect. The transient resistance during the oscillatory motion therefore is $\mathcal{F}_{\mathrm{cM}} = \tilde{\mathcal{F}}_{\mathrm{cM}}(\beta, \mathrm{De}, \alpha, d)e^{it}$, where the local viscosity α and depletion thickness d are accounted for by computation of $f''(1)$ and $f'''(1)$. For a uniform Newtonian fluid with a finite β value, $f''(1) = 1/2 - 3ki/2$ and $f'''(1) = -3/2 + 3k^2/2 + 3ki/2$, where $k = (i-1)\sqrt{\beta/2\alpha}$, $\beta = \rho\omega R_c^2/\eta_s$, and $\alpha = \eta_0/\eta_s$. The resulting formulation and numerical results are consistent with the quasistationary approximation in Newtonian fluids [62] as $\beta \to 0$ and $\mathrm{De} \to 0$.

D. Limiting cases

(i) For a single-mode uniform Maxwell fluid, $A = 0$ and complex wave vector $k^{(\mathrm{i})} = k^{(\mathrm{o})} = k_{\mathrm{M}} = (i-1)\sqrt{\beta(1+i\mathrm{De})/(2\alpha_b)}$, where the ratio of zero-frequency to solvent viscosity α_b is a constant. Furthermore, $a^{(\mathrm{i})} = a^{(\mathrm{o})} = -3e^{-ik_{\mathrm{M}}}/(2ik_{\mathrm{M}})$, $b^{(\mathrm{i})} = b^{(\mathrm{o})} = -(1 - 3/ik_{\mathrm{M}} - 3/{k_{\mathrm{M}}}^2)/2$, $c^{(\mathrm{i})} = 0$, and the complex amplitude of the total drag reduces to

$$\tilde{\mathcal{F}}_{\mathrm{M}} = -\alpha_b\overline{\eta}^*_{\mathrm{M}}\left(1 - ik_{\mathrm{M}} - \tfrac{1}{9}k_{\mathrm{M}}^2\right), \tag{56}$$

where $\alpha_b\overline{\eta}^*_{\mathrm{M}}$ is the scaled complex viscosity and $\overline{\eta}^*_{\mathrm{M}}$ is defined by Eq. (18).

(ii) In case of depletion of Newtonian polymer solutions, the two-layer approximation of Newtonian fluids leads to $\mathrm{De} = 0$, $k^{(\mathrm{i})} = (i-1)\sqrt{\beta/2\alpha^{(\mathrm{i})}}$, and $k^{(\mathrm{o})} = (i-1)\sqrt{\beta/2\alpha^{(\mathrm{o})}}$. The viscosity ratio $\alpha^{(\mathrm{i})} = 1$ for the viscosity of the depletion zone simply approximated by solvent viscosity, and $\alpha^{(\mathrm{o})} = \alpha_b$. For a special case of uniform Newtonian fluid, both the constants A and Deborah number De vanish, and $k^{(\mathrm{i})} = k^{(\mathrm{o})} = k_{\mathrm{N}} = (i-1)\sqrt{\beta/2\alpha_b}$. Also $a^{(\mathrm{i})} = -3e^{-ik_{\mathrm{N}}}/(2ik_{\mathrm{N}})$, $b^{(\mathrm{i})} = -(1 - 3/ik_{\mathrm{N}} - 3/{k_{\mathrm{N}}}^2)/2$, $a^{(\mathrm{o})} = a^{(\mathrm{i})}$, $b^{(\mathrm{o})} = b^{(\mathrm{i})}$, $c^{(\mathrm{i})} = 0$, and the drag amplitude [78] becomes

$$\tilde{\mathcal{F}}_{\mathrm{N}} = -\alpha_b\left(1 - ik_{\mathrm{N}} - \tfrac{1}{9}k_{\mathrm{N}}^2\right). \tag{57}$$

The first term in parentheses represents the typical Stokes drag contributed by both pressure and shear viscous stress on surface. The k_{N} term is known as the Basset history effect relevant to both particle velocity and acceleration, also contributed to by flow pressure and shear stress acting on the particle surface. The k_{N}^2 term is known as the added or additional effective-mass effect which only comes from pressure and is related to the acceleration of the particle. A similar mathematical form can be cast for uniform Maxwell fluid with stress relaxation taken into account.

(iii) In the quasisteady or zero-frequency limit, $\beta \to 0$ and $\mathrm{De} \to 0$, $k^{(\mathrm{i})} = k^{(\mathrm{o})} = 0$, the total drag of the two-layer model [61] reduces to

$$\mathcal{F}_{2\mathrm{s}} = -\left[2\left(2+\frac{3}{\alpha}\right)d_{\mathrm{s}}^{6} - 4\left(1-\frac{1}{\alpha}\right)d_{\mathrm{s}}\right]\Big/\Gamma, \tag{58}$$

where $d_{\mathrm{s}} = 1 + d$, and $\Gamma = 2(2+3/\alpha)d_{\mathrm{s}}^{6} - 3(3+2/\alpha)(1-1/\alpha)d_{\mathrm{s}}^{5} + 10(1-1/\alpha)d_{\mathrm{s}}^{3} - 9(1-1/\alpha)d_{\mathrm{s}} + 4(1-1/\alpha)^{2}$.

Next, we demonstrate the transient flow patterns and the apparent complex viscosity sensed by the particle to distinguish the apparent value from the actual viscosity of the bulk fluid. The roles of dimensionless parameters including viscosity ratio α, frequency parameter β, Deborah number De, and the apparent depletion thickness d are discussed.

III. RESULTS AND DISCUSSION

Figure 3 demonstrates the streamlines and contour map for the scaled velocity magnitude on the transient flow driven by a vertically oscillating sphere. The cases include a uniform Newtonian fluid with bulk-to-solvent viscosity ratio $\alpha_b = 100$ and a frequency parameter $\beta = 1$ [Fig. 3(a)], a nonuniform Newtonian fluid with $\alpha_b = 100$, $\beta = 1$, and a depletion thickness $d = 1$ [Fig. 3(b)], a uniform Maxwell fluid with $\alpha_b = 100$, $\beta = 1$, Deborah number $\mathrm{De} = 100$ [Fig. 3(c)], and a nonuniform Maxwell fluid with $\alpha_b = 100$, $\beta = 1$, $\mathrm{De} = 100$, and $d = 1$ [Fig. 3(d)]. The nonuniform cases 3(b) and 3(d) are obtained from the numerical model presented above. The local acceleration of the fluid is significant and the transient flow constantly evolves with a toroidal vortex initiated periodically at the particle surface. The Newtonian fluids [Figs. 3(a) and 3(b)] have a typical diffusive behavior showing viscous dissipation into the nearby domain, while the Maxwell fluids [Figs. 3(c) and 3(d)] exhibit a mixed diffusive and elastic behavior with an oscillatory diffusion wave expanding and propagating laterally into the far field. The sustained elastic wave on top of the migrating toroidal vortex is formed by alternating circulations around the particle. A spatially oscillatory pattern reveals itself clearly. The structure with higher wave number, which is proportional to the square root of the Deborah number, is due to the longer stress relaxation time. Furthermore, comparing the depletion cases [Figs. 3(b) and 3(d)] with uniform cases [Figs. 3(a) and 3(c)], because of the much lower viscosity within the depletion zone, the flow is relatively confined within the depletion zone [Figs. 3(b) and 3(d)] and the velocity quickly damps out in the bulk. Under the same bulk properties, cases with depletion are expected to have less dissipation loss and smaller resistance to the particle motion. A small toroidal circulation that appears in the depletion zone from time to time during the periodic motion is similar to the cage effect due to the high viscosity ratio.

Figures 4(a)–4(d) compare the two-layer analytical approximation with the numerical result [Figs. 4(a′)–4(d′)] of the continuous model on a transient Maxwell fluid flow induced by a vertically oscillating sphere. Streamlines and scaled velocity magnitude for approximately a quarter of the cycle are shown, starting from the instant that the sphere reverses its moving direction [Fig. 4(a)]. The toroidal vortex is first introduced at the turn of the moving direction and is attached to the sphere's surface [Fig. 4(b)] while the rest of the domain is not yet perturbed due to the lag of inertial effect. In the later stages the vortex expands and migrates laterally [Figs. 4(c) and 4(d)] and dissipates into the far field. The flow gradually changes its direction completely from nearby to the far field [Figs. 4(a) and 4(d)], followed by the next quarter of the cycle. At the end of the half cycle the vortex dissipates and velocity decays significantly, and a new vortex is about to appear right after the reversal of the moving direction. Higher velocity appears near the north and south poles of the sphere most of the time, as expected. In this case, at frequency parameter $\beta = 1$, the transient flow already deviates significantly from the stationary Stokes flow. The elastic effect is relatively weak ($\mathrm{De} = 10$) and the bulk-to-solvent viscosity ratio ($\alpha_b = 10$) is low to represent an unentangled, dilute polymer solution, so that the overall flow patterns are very similar to a uniform Maxwell fluid

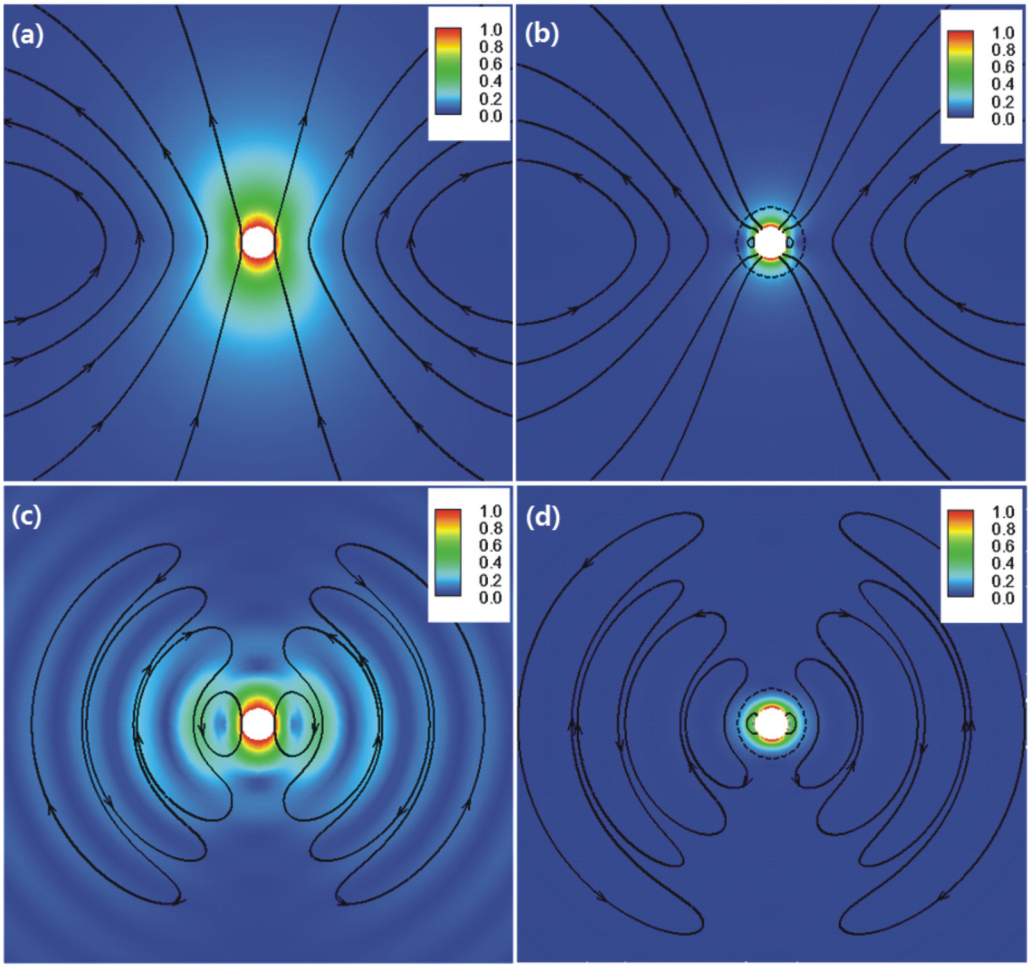

FIG. 3. Instantaneous flow patterns near the reversal point of the moving direction, showing streamlines and contour map of scaled velocity magnitude in polymer solutions (b), (d) with and (a), (c) without polymer depletion effect. (a), (b) Newtonian fluids are compared with (c), (d) Maxwell viscoelastic fluids. Parameters used are listed in text. The dashed line appearing in panels (b) and (d) gives the location of the depletion interface at $r = 1 + d$.

except in the near-field region. The depletion thickness, $d = 1$, is about the particle radius, and the depletion zone can be observed from the slightly distorted streamlines across the depletion interface. Steeply connected [Figs. 4(c) and 4(d)] versus smooth [Figs. 4(c′) and 4(d′)] streamlines appear at the interface, indicating the difference between two-layer and continuous approximations of the flow field. In the limiting case where $\beta \to 0$ and $\mathrm{De} \to 0$, the resulting flow pattern is consistent with the quasisteady model [61,62].

In Fig. 5 we compare the velocity profiles extending from the equator ($\theta = \pi/2$) of the oscillating sphere at various bulk-to-solvent viscosity ratios, Deborah numbers, and depletion thicknesses. The two-layer approximation agrees well with the continuous model for cases with (i) a relatively thin depletion thickness, where particle size is relatively large compared with the polymer radius of gyration or polymer correlation length, and (ii) a relatively small bulk-to-solvent viscosity ratio that corresponds to dilute polymer solutions. Near the particle surface the velocity gradient based on both models are very close to each other so that the two-layer analytical result provides a

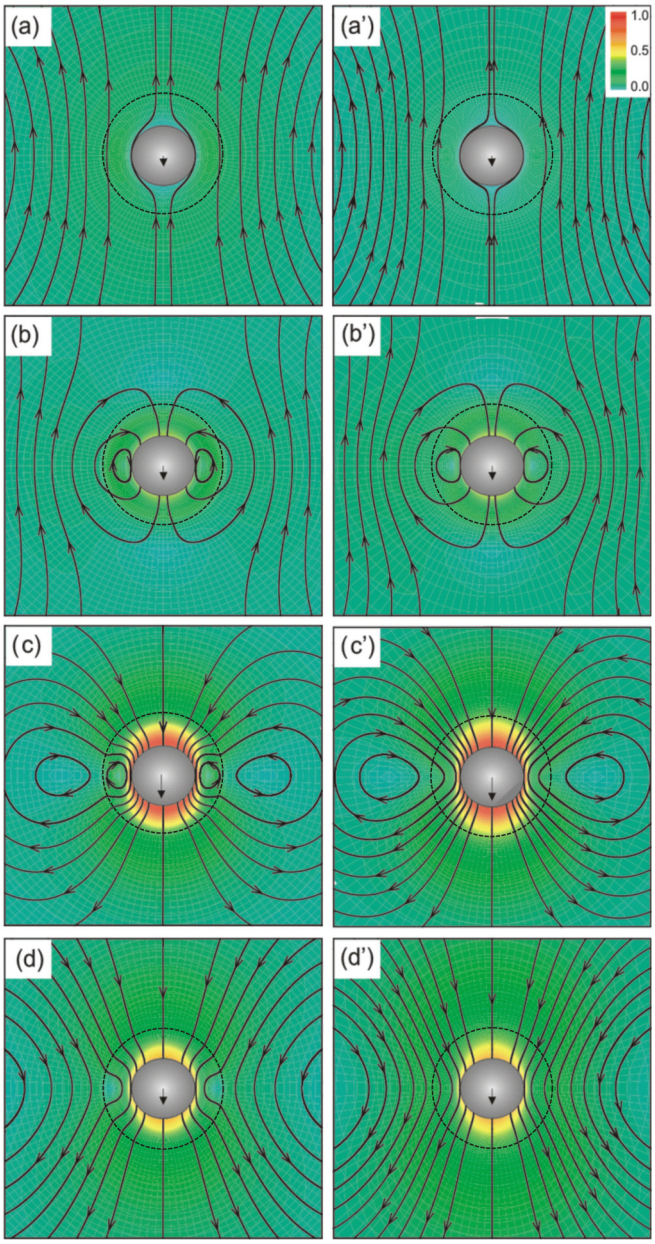

FIG. 4. Streamlines and scaled velocity amplitude around a vertically oscillating sphere in a linear viscoelastic fluid with bulk-to-solvent viscosity ratio $\alpha_b = 10$, frequency parameter $\beta = 1$, Deborah number $\mathrm{De} = 10$, and apparent depletion thickness $d = 1$. Left and right panels are the corresponding two-layer and continuous models, respectively, at four scaled time instants: (a), (a′) $t = 0.5\pi$, (b), (b′) 0.53π, (c), (c′) 0.6π, and (d), (d′) 0.9π. The scaled period $T = 2\pi$. At $t = 0$ the particle is located at the mean position of the oscillation. Dashed lines indicate the depletion interface at $r = 1 + d$.

reasonable estimation of resistance that the sphere experiences, as long as the depletion thickness is approximately less than 1. In the semidilute regime with higher viscosity ratio, the deviation between the two models near the depletion zone increases; see the comparison in Fig. 5(c). The continuous model has a more realistic smooth transition for the circulation from the particle

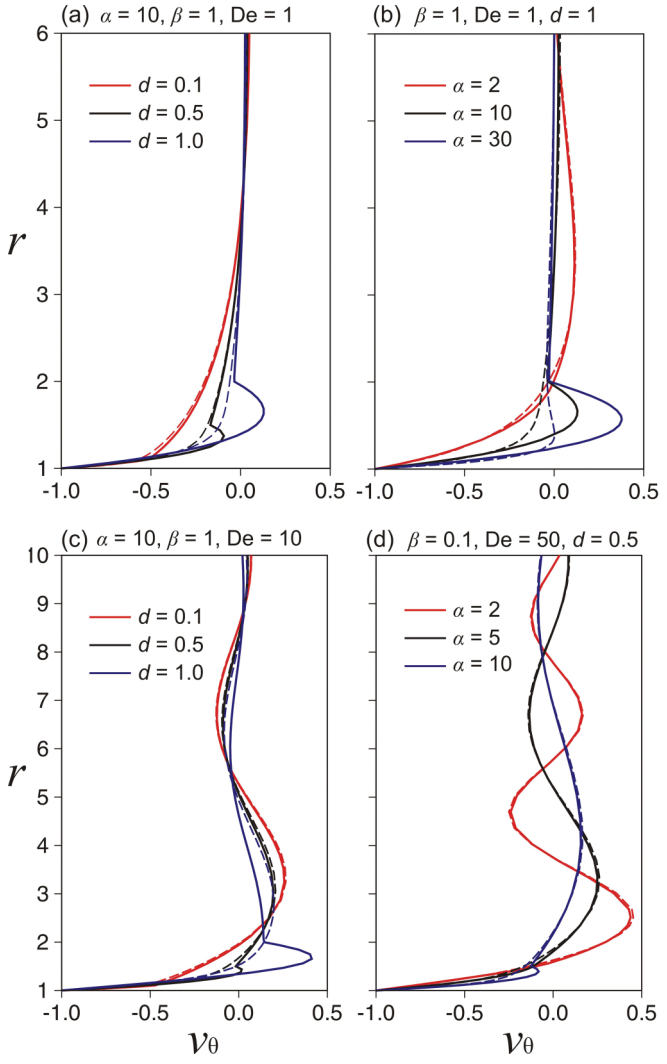

FIG. 5. Comparison of velocity profiles based on two-layer (solid lines) and continuous (dashed lines) models at $\theta = \pi/2$ and $1 \leqslant r \leqslant 6$ to 10, at the time instant when the sphere passes through its mean position. Parameters are listed in the figure.

surface to the depletion interface, while under the same apparent depletion thickness the two-layer approximation requires a larger circulation in the depletion zone in order to satisfy the coupled dynamic boundary conditions at the depletion interface. At lower viscosity ratio the scaled velocity magnitude has a larger domain of influence, while at large viscosity ratio the velocity variation is relatively confined within the depletion zone. Comparing Fig. 5(a) with Fig. 5(c), it is observed that, at higher Deborah number, the velocity profiles oscillate a few times before vanishing into the far field, which is consistent with the elastic-diffusive waves observed earlier with alternating toroidal vortices expanding and propagating into the far field. In Fig. 5(d) we consider a case with dimensionless parameters based on, for example, a dilute solution with a polymer radius of gyration slightly smaller than the particle size, $d \simeq 0.5$, a solution mass density $\rho \simeq 10^3$ kg m^{-3}, a solvent viscosity $\eta_s \simeq 10^{-3}$ Pa s, a particle radius $R = 1$ μm, a driving frequency $\omega = 10^5$ rad s^{-1}, and a solution stress relaxation time $\lambda = 5 \times 10^{-4}$ s and thus De $= 50$, or another example with a

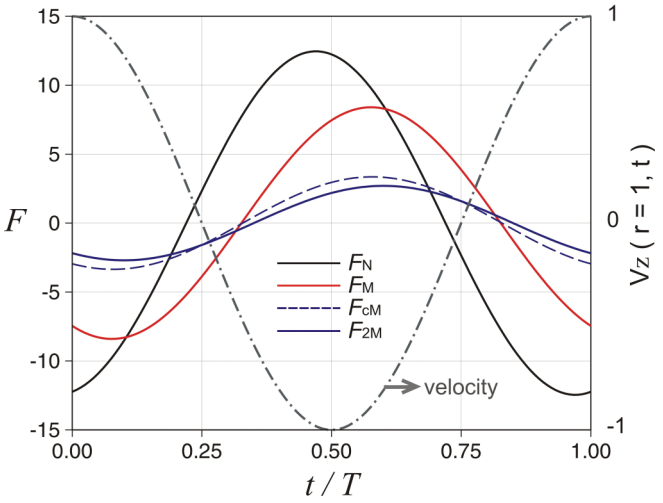

FIG. 6. Scaled transient resistance acting on a translationally oscillating sphere versus time. The dash-dotted line indicates the scaled velocity $\boldsymbol{v}(r=1,t)\cdot\hat{\mathbf{e}}_z$ of the sphere as a reference for comparing the phase behaviors. Subscript "N" indicates uniform Newtonian fluid, "M" for uniform Maxwell fluid, "cM" for nonuniform Maxwell fluid with continuous concentration profile, and "2M" for two-layer Maxwell fluid. Only the real part of the complex drag force is shown for the force models with $\alpha_b = 10$ and $\beta = 1$. Deborah number $\mathrm{De} = 1$ for all Maxwell models, and the characteristic depletion thickness $d = 1$ is used for both continuous and two-layer Maxwell models. T is the oscillation period.

relatively large colloidal sphere with $R = 10\ \mu$m, $\omega = 10^3$ rad s^{-1}, and $\lambda = 5\times10^{-2}$ s. In these cases, the velocity profiles predicted by both the two-layer and continuous models are consistent with each other within the fluid domain. At lower viscosity ratio α, the depth of viscous penetration, given by Eq. (25), is relatively short, resulting in a higher wave number k, and thereby more oscillation appears in space, as shown in Fig. 5(d).

Figure 6 compares the modeling results of transient resistance based on the same viscosity ratio and Deborah number. The resistance can be obtained by taking the real part of the scaled complex drag, $\mathcal{F} = \mathrm{Re}[\tilde{\mathcal{F}}e^{it}]$, which carries a phase lag relative to the particle's velocity. Under the same particle size and polymer conditions, overall the particle experiences the highest drag in uniform Newtonian fluid $\tilde{\mathcal{F}}_\mathrm{N}$ for a given viscosity ratio α_b, which has a phase difference close to but not equal to π relative to the particle velocity due to the inertial effect in the transient flow. The uniform Maxwell fluid has a phase lag, $\pi/4$, compared with the uniform Newtonian model because $\mathrm{De} = 1$ and the loss tangent of the lag is $\tan\delta = \mathrm{De}^{-1} = 1$. At significant depletion thickness $d = 1$, both the continuous and two-layer models have significant reduction of the overall resistance force compared with the uniform Maxwell model. This is similar to an effective slip mediated by the depletion zone [61,84]. Such deviation increases as the viscosity ratio and depletion thickness increase. The forces $\mathcal{F}_\mathrm{M}$ and $\mathcal{F}_\mathrm{cM}$ are in phase under the same Deborah number. The two-layer model slightly underpredicts the resistance. The solvent inner layer has no elastic effect, which causes a small phase lag compared with the uniform or continuous model.

From an experimental perspective, for a given particle size, fluid density, solvent viscosity, driving frequency, and a nonadsorbing polymer solution described by α_b, d, and De, the apparent complex viscosity to be sensed by an oscillating sphere can be casted into a form derived for the single-mode uniform Maxwell fluid, Eq. (56), and formulated as

$$\frac{\eta^*_\mathrm{M}}{\eta_s} = \frac{-\tilde{\mathcal{F}}_\mathrm{M}}{1-ik-k^2/9},\quad \frac{\eta^*_\mathrm{2M}}{\eta_s} = \frac{-\tilde{\mathcal{F}}_\mathrm{2M}}{1-ik-k^2/9},\quad \frac{\eta^*_\mathrm{cM}}{\eta_s} = \frac{-\tilde{\mathcal{F}}_\mathrm{cM}}{1-ik-k^2/9}, \tag{59}$$

where the complex viscosity is scaled by the solvent viscosity η_s. The complex wave number is given by

$$k(\alpha_b, \beta, \mathrm{De}) = (i-1)\sqrt{\frac{\beta}{2\alpha_b \overline{\eta}^*}} = (i-1)\sqrt{\frac{\beta}{2\alpha_b}(1+i\mathrm{De})}. \tag{60}$$

Presumably, $\tilde{\mathcal{F}}_{\mathrm{M}}$ is the force amplitude in an assumed uniform Maxwell fluid that one may hope to measure directly by using the colloidal probe, and $\tilde{\mathcal{F}}_{2\mathrm{M}}$ and $\tilde{\mathcal{F}}_{\mathrm{cM}}$ are the more realistic amplitudes of the corresponding resistances with the polymer depletion effect taken into account. The theoretical model would help to better understand the deviation between the inferred and true bulk properties.

Figure 7(a) demonstrates the numerical results of $(\bar{\eta}^*_{\mathrm{cM}})$ under various depletion thicknesses with $\alpha_b = 10$, $\beta = 0.01$, and De ranging from 10^{-1} to 30. For example, $\rho \simeq 10^3$ kg m^{-3}, $\eta_{\mathrm{s}} \simeq 10^{-3}$ Pa s, $R = 1$ μm, $\omega = 10^4$ s^{-1}, and the stress relaxation time of the sample polymer solution ranges from $\lambda = 10^{-5}$ to 3×10^{-3} s. Three cases with scaled depletion thicknesses, $d = 0.1$, 0.5, and 1.0 are computed to compare with the corresponding uniform Maxwell model without depletion. The intercepts of solid and dashed lines are the corresponding crossover points where De $\simeq 1$ and $\eta' = \eta''$ for a small β value 0.01. It is found that the deviation of the apparent versus true viscosity in the bulk can be significant, especially when the depletion thickness is large. In the demonstrated case, a thickness of only 10% of the particle radius corresponds to a reduction of about 20% of the complex viscosity at low De. At low Deborah number (fluid-like material) the numerical results using continuous viscosity profiles are compared with the corresponding two-layer Newtonian model. The three asymptotes (dash-dotted lines) for De $\to 0$ are obtained from the two-layer Newtonian model, Eq. (58). As expected, the simplified two-layer model slightly overpredicts the reduction of η', but is fairly accurate as d is approximately less than 0.5. Note that the crossover viscosity does not recover to α_b as $d \to 0$ due to the apparent slip effect at the nonadsorbing surface [61]. Figure 7(b) shows the sensitivity tests on the frequency parameter β. The crossover viscosity shifts to a Deborah number De < 1 as β increases. This is due to inertial contribution to the imaginary part of the drag force. At a higher β the inertial effect is stronger; for example, as the probe size increases, η'' increases slightly as η' decreases, and the crossover viscosity corresponds to a lower Deborah number. However, the inertial effect is convoluted with the apparent slip phenomena because higher β also enhances the apparent slip effect due to depletion, which reduces the complex viscosity.

If the elastic energy in the polymer solutions comes from several sources, phenomenologically the general Maxwell model with multiple relaxation modes is more flexible for analyzing the experimental data. Figures 8(a) demonstrates that the depletion effect can be resolved for each mode of the general Maxwell model. The overall contribution of discrete viscosity is obtained from the assumed three-scale Maxwell model with the discrete relaxation times defined based on the Rouse model, Eqs. (8) and (9). The higher mode has less contribution at low Deborah number, and more in the high-Deborah-number regime, as expected, and the three crossover points correspond to the discrete relaxation times. Figure 8(b) shows the sensitivity tests on the zero-shear viscosity α_b from 2 to 100 in the bulk with a relative large depletion thickness $d = 1$.

Furthermore, experimentally, if the monochromatic resistance (rather than full-spectrum response in Brownian motion) acting on the oscillatory sphere is directly measured, in principle, an inverse formulation can be applied to extract the unknown zero-frequency viscosity ratio α_b and the sample relaxation time λ, and thus to obtain the actual complex viscosity that represents the bulk material. The inverse formulations based on the two-layer and continuous models, Eqs. (38) and (55), however, are implicit formulations of α_b and De. They may be determined by monochromatic measurement of force amplitude and phase lag by using optical or magnetic tweezers. The zero-frequency viscosity α_b can be measured at $\omega \to 0$ and be predicted by the stationary model in the Newtonian limit, such as Eq. (58). Oftentimes, microrheology experiments are performed on a passive mode. Either the mean square displacement of the trajectory of the Brownian particle or the autocorrelation of the scattering light intensity is recorded to approximate the self diffusivity of the

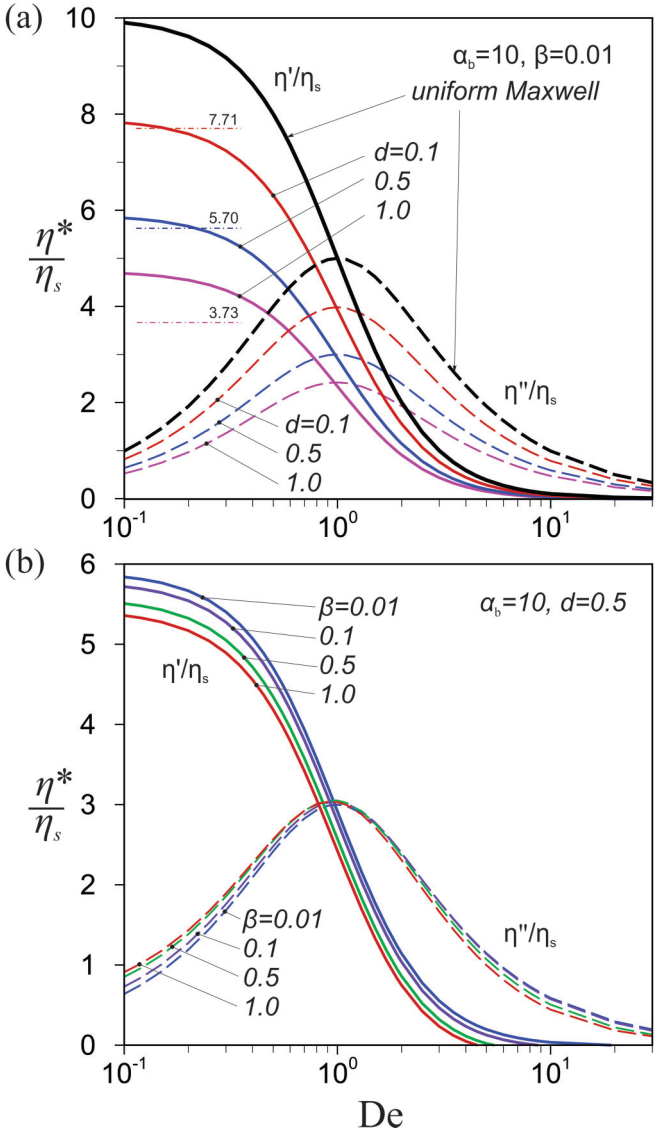

FIG. 7. Reduction of resistance due to the presence of the depletion zone represented by the scaled apparent complex viscosity $\eta^*/\eta_s = (\eta' - i\eta'')/\eta_s$, where η_s is the viscosity of a pure solvent. The solid curves represent η'/η_s, whereas the dashed curves represent the corresponding η''/η_s values. (a) Comparison of uniform (no depletion), two-layer model as De $\to$ 0 (dash-dotted lines), and continuous Maxwell models at $\alpha = 10$, $\beta = 0.01$, and $d = 0.1$, 0.5, and 1.0. (b) Comparison of cases with $\alpha = 10$, $d = 0.5$, and β from 0.01 to 1.0.

particle. The resistance data involve the contribution from the whole spectrum. In principle they can be transformed to the frequency domain to obtain the monochromatic complex viscosity based on the general Stokes-Einstein relation [3,4,8,9,85]. At the lower frequency range where inertial effects are negligible, the complex viscosity $\eta^*_{\rm eff}(\omega) \simeq k_B T/[-\pi R\omega^2\langle\Delta\mathbf{r}^2(\omega)\rangle]$, where $\eta^*_{\rm eff}$ corresponds to $\eta^*_{\rm 2M}$ or $\eta^*_{\rm cM}$ in our models. Inferring the spectral relaxation times of linear viscoelastic materials from experimental data is an inverse problem that may rely on additional dynamic regression and inference analysis [86–88]. Further investigation is needed to validate the proposed theoretical

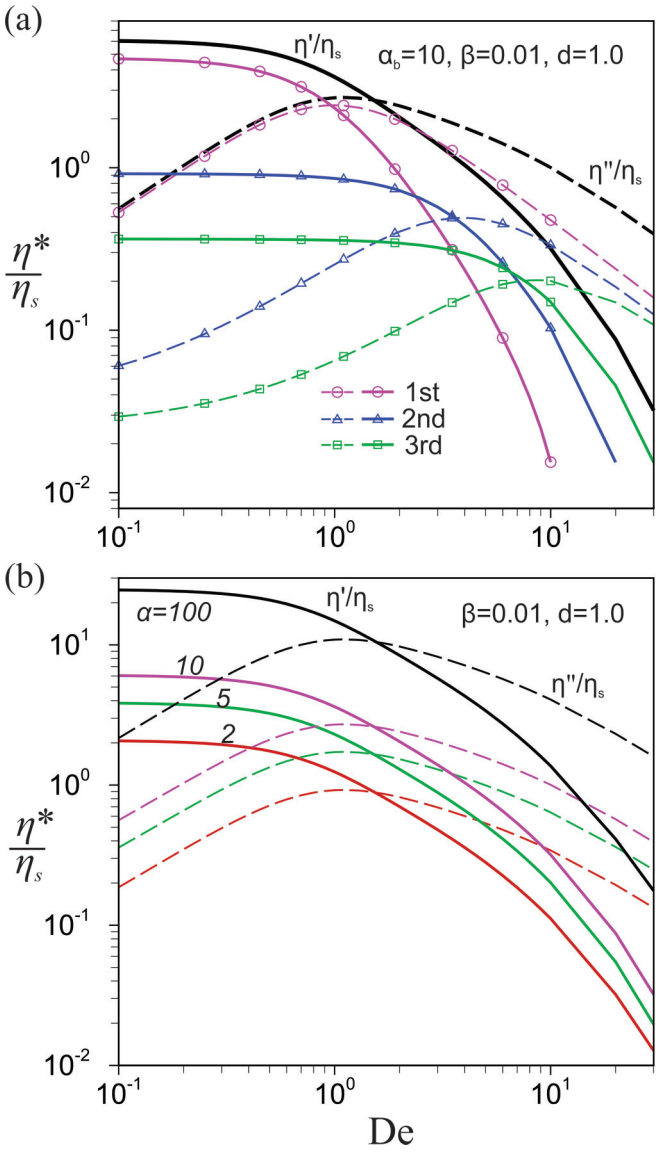

FIG. 8. Depletion effect on the general Maxwell model in terms of the scaled complex viscosity versus Deborah number. (a) The solid and dashed lines represent η'/η_s and η''/η_s, respectively, and the contributions of the three individual modes with discrete relaxation times λ_j defined in Eq. (9) at $\alpha_b = 10$, $\beta = 0.01$, and $d = 1$. (b) Comparison of apparent complex viscosity at various bulk values of α_b and at $\beta = 0.01$ and $d = 1$.

models in terms of apparent complex viscosity and the corresponding spectral relaxation times under various polymer conditions.

IV. CONCLUSION

A theoretical approach is presented to describe viscoelastic flow induced by monochromatic, small-amplitude, translational oscillatory motion of a colloidal sphere in nonadsorbing polymer solutions. The viscoelastic flow patterns influenced by local inhomogeneity and stress relaxation

are revealed in detail, and the overall drag coefficient and the corresponding apparent complex viscosity are quantified based on the general Maxwell model. The models aim for local analysis of microrheological measurements of complex fluids using active and passive colloidal probing methods.

ACKNOWLEDGMENTS

Y.H. and T.-H.F. acknowledge financial support from NSF, Grant No. CMMI-0952646, T.T. acknowledges support from KAKENHI, Grant No. 15K13549.

[1] D. T. N. Chen, Q. Wen, P. A. Janmey, J. C. Crocker, and A. G. Yodh, Rheology of soft materials, Annu. Rev. Condens. Matter Phys. **1**, 301 (2010).
[2] D. J. Pine, D. A. Weitz, P. M. Chaikin, and E. Herbolzheimer, Diffusing-Wave Spectroscopy, Phys. Rev. Lett. **60**, 1134 (1988).
[3] T. G. Mason and D. A. Weitz, Optical Measurements of Frequency-Dependent Linear Viscoelastic Moduli of Complex Fluids, Phys. Rev. Lett. **74**, 1250 (1995).
[4] T. G. Mason, H. Gang, and D. A. Weitz, Rheology of complex fluids measured by dynamic light scattering, J. Mol. Struct. **383**, 81 (1996).
[5] F. Gittes, B. Schnurr, P. D. Olmsted, F. C. MacKintosh, and C. F. Schmidt, Microscopic Viscoelasticity: Shear Moduli of Soft Materials Determined from Thermal Fluctuations, Phys. Rev. Lett. **79**, 3286 (1997).
[6] M. J. Solomon and Q. Lu, Rheology and dynamics of particles in viscoelastic media, Curr. Opin. Colloid Interface Sci. **6**, 430 (2001).
[7] B. R. Dasgupta, S.-Y. Tee, J. C. Crocker, B. J. Frisken, and D. A. Weitz, Microrheology of polyethylene oxide using diffusing wave spectroscopy and single scattering, Phys. Rev. E **65**, 051505 (2002).
[8] T. A. Waigh, Microrheology of complex fluids, Rep. Prog. Phys. **68**, 685 (2005).
[9] T. M. Squires and T. G. Mason, Fluid mechanics of microrheology, Annu. Rev. Fluid Mech. **42**, 413 (2010).
[10] R. N. Zia, Active and passive microrheology: Theory and simulation, Annu. Rev. Fluid Mech. **50**, 371 (2018).
[11] J. Mewis and N. J. Wagner, *Colloidal Suspension Rheology* (Cambridge University Press, New York, 2012).
[12] B. Cichocki and B. U. Felderhof, Linear viscoelasticity of semidilute hard-sphere suspensions, Phys. Rev. A **43**, 5405 (1991).
[13] J. F. Brady, The rheological behavior of concentrated colloidal dispersions, J. Chem. Phys. **99**, 567 (1993).
[14] R. A. Lionberger and W. B. Russel, High frequency modulus of hard sphere colloids, J. Rheol. (Melville, NY, US) **38**, 1885 (1994).
[15] J. F. Brady and J. F. Morris, Microstructure of strongly sheared suspensions and its impact on rheology and diffusion, J. Fluid Mech. **348**, 103 (1997).
[16] G. Nägele and J. Bergenholtz, Linear viscoelasticity of colloidal mixtures, J. Chem. Phys. **108**, 9893 (1998).
[17] G. Nägele, Viscoelasticity and diffusional properties of colloidal model dispersions, J. Phys.: Condens. Matter **15**, S407 (2003).
[18] I. Sriram, E. M. Furst, R. J. DePuit, and T. M. Squires, Small amplitude active oscillatory microrheology of colloidal suspension, J. Rheol. (Melville, NY, US) **53**, 357 (2009).
[19] I. Sriram, A. Meyer, and E. M. Furst, Active mirorheology of a colloidal suspension in the direct collision limit, Phys. Fluids **22**, 062003 (2010).
[20] R. N. Zia and J. F. Brady, Stress development, relaxation, and memory in colloidal dispersions: Transient nonlinear microrheology, J. Rheol. (Melville, NY, US) **57**, 457 (2013).
[21] J. W. Swan, R. N. Zia, and J. F. Brady, Large amplitude oscillatory microrheology, J. Rheol. (Melville, NY, US) **58**, 1 (2014).

[22] J. W. Swan, E. M. Furst, and N. J. Wagner, The medium amplitude oscillatory shear of semi-dilute colloidal dispersions. Part I: Linear response and normal stress differences, J. Rheol. (Melville, NY, US) **58**, 307 (2014).
[23] N. J. Hoh and R. N. Zia, Hydrodynamic diffusion in active microrheology of non-colloidal suspensions: The role of interparticle forces, J. Fluid Mech. **785**, 189 (2015).
[24] H. C. W. Chu and R. N. Zia, Active microrheology of hydrodynamically interacting colloids: Normal stresses and entropic energy density, J. Rheol. (Melville, NY, US) **60**, 755 (2016).
[25] G. Wang and J. W. Swan, Large amplitude oscillatory shear of hard-sphere colloidal dispersions: Brownian dynamics simulation and fourier-transform rheology, J. Rheol. (Melville, NY, US) **60**, 1041 (2016).
[26] E. Nazockdast and J. F. Morris, Active microrheology of colloidal suspensions: Simulation and microstructural theory, J. Rheol. (Melville, NY, US) **60**, 733 (2016).
[27] J. D. Park, K. H. Ahn, and N. J. Wagner, Structural-rheology relationship for a homogeneous colloidal gel under shear startup, J. Rheol. (Melville, NY, US) **61**, 117 (2017).
[28] S. Marenne and J. F. Morris, Nonlinear rheology of colloidal suspensions probed by oscillatory shear, J. Rheol. (Melville, NY, US) **61**, 797 (2017).
[29] T. G. Mason, Estimating the viscoelastic moduli of complex fluids using the generalized stokes-Einstein equation, Rheol. Acta **39**, 371 (2000).
[30] J. C. Crocker, M. T. Valentine, E. R. Weeks, T. Gisler, P. D. Kaplan, A. G. Yodh, and D. A. Weitz, Two-Point Microrheology of Inhomogeneous Soft Materials, Phys. Rev. Lett. **85**, 888 (2000).
[31] A. J. Levine and T. C. Lubensky, One- and Two-Particle Microrheology, Phys. Rev. Lett. **85**, 1774 (2000).
[32] A. J. Levine and T. C. Lubensky, Two-point microrheology and the electrostatic analogy, Phys. Rev. E **65**, 011501 (2001).
[33] A. J. Levine and T. C. Lubensky, Response function of a sphere in a viscoelastic two-fluid medium, Phys. Rev. E **63**, 041510 (2001).
[34] D. T. Chen, E. R. Weeks, J. C. Crocker, M. F. Islam, R. Verma, J. Gruber, A. J. Levine, T. C. Lubensky, and A. G. Yodh, Rheological Microscopy: Local Mechanical Properties from Microrheology, Phys. Rev. Lett. **90**, 108301 (2003).
[35] S. B. Zimmerman and A. P. Minton, Macromolecular crowding: Biochemical, biophysical, and physiological consequences, Annu. Rev. Biophys. Biomol. Struct. **22**, 27 (1993).
[36] L. Starrs and P. Bartlett, Colloidal dynamics in polymer solutions: Optical two-point microrheology measurements, Faraday Discuss. **123**, 323 (2002).
[37] M. Karzar-Jeddi, R. Tuinier, T. Taniguchi, and T.-H. Fan, Stochastic interactions of two Brownian hard spheres in the presence of depletants, J. Chem. Phys. **140**, 214906 (2014).
[38] S. Asakura and F. Oosawa, On interaction between two bodies immersed in a solution of macromolecules, J. Chem. Phys. **22**, 1255 (1954).
[39] S. Asakura and F. Oosawa, Interaction between particles suspended in solutions of macromolecules, J. Polym. Sci. **33**, 183 (1958).
[40] A. Vrij, Polymers at interfaces and the interactions in colloidal dispersions, Pure Appl. Chem. **48**, 471 (1976).
[41] A. P. Gast, C. K. Hall, and W. B. Russel, Polymer-induced phase separations in nonaqueous colloidal suspensions, J. Colloid Interface Sci. **96**, 251 (1983).
[42] H. N. W. Lekkerkerker, W. C.-K. Poon, P. N. Pusey, A. Stroobants, and P. B. Warren, Phase behavior of colloid + polymer mixtures, Europhys. Lett. **20**, 559 (1992).
[43] G. Fleer, M. A. Cohen Stuart, J. M. H. M. Scheutjens, T. Cosgrove, and B. Vincent, *Polymers at Interfaces* (Springer, 1993).
[44] K. S. Schweizer and J. G. Curro, PRISM theory of the structure, thermodynamics, and phase transitions of polymer liquids and alloys, Adv. Polym. Sci. **116**, 319 (1994).
[45] G. J. Fleer, A. M. Skvortsov, and R. Tuinier, Mean-field equation for the depletion thickness, Macromolecules (Washington, DC, US) **36**, 7857 (2003).

[46] Y.-L. Chen, K. S. Schweizer, and M. Fuchs, Phase separation in suspensions of colloids, polymers and nanoparticles: Role of solvent quality, physical mesh, and nonlocal entropic repulsion, J. Chem. Phys. **118**, 3880 (2003).
[47] H. N. W. Lekkerkerker and R. Tuinier, *Colloids and the Depletion Interaction* (Springer, Dordrecht, 2011).
[48] K. Yaman, C. Jeppesen, and C. M. Marques, Depletion forces between two spheres in a rod solution, Europhys. Lett. **42**, 221 (1998).
[49] K.-H. Lin, J. C. Crocker, A. C. Zeri, and A. G. Yodh, Colloidal Interactions in Suspensions of Rods, Phys. Rev. Lett. **87**, 088301 (2001).
[50] Y.-L. Chen and K. S. Schweizer, Liquid-state theory of structure, thermodynamics, and phase separation in suspensions of rod polymers and hard spheres, J. Phys. Chem. B **108**, 6687 (2004).
[51] R. Tuinier, T.-H. Fan, and T. Taniguchi, Depletion and the dynamics in colloid-polymer mixtures, Curr. Opin. Colloid Interface Sci. **20**, 66 (2015).
[52] T.-H. Lin and G. D. J. Phillies, Translational diffusion coefficient of a macroparticulate probe species in salt-free poly(acrylic acid)-water, J. Phys. Chem. **86**, 4073 (1982).
[53] R. I. Cukier, Diffusion of Brownian spheres in semidilute polymer solutions, Macromolecules (Washington, DC, US) **17**, 252 (1984).
[54] G. S. Ullmann, K. Ullmann, R. M. Lindner, and G. D. J. Phillies, Probe diffusion of polystyrene latex spheres in poly(ethylene oxide)-water, J. Phys. Chem. **89**, 692 (1985).
[55] K. L. Ngai and G. D. J. Phillies, Coupling model analysis of polymer dynamics in solution: Probe diffusion and viscosity, J. Chem. Phys. **105**, 8385 (1996).
[56] X. Ye, P. Tong, and L. J. Fetters, Transport of probe particles in semidilute polymer solutions, Macromolecules (Washington, DC, US) **31**, 5785 (1998).
[57] Y. Cheng, R. K. Prud'homme, and J. L. Thomas, Diffusion of mesoscopic probes in aqueous polymer solutions measured by fluorescence recovery after photobleaching, Macromolecules (Washington, DC, US) **35**, 8111 (2002).
[58] T. Odijk, Depletion theory of protein transport in semi-dilute polymer solutions, Biophys. J. **79**, 2314 (2000).
[59] G. H. Koenderink, S. Sacanna, D. G. A. L. Aarts, and A. P. Philipse, Rotational and translational diffusion of fluorocarbon tracer spheres in semidilute xanthan solutions, Phys. Rev. E **69**, 021804 (2004).
[60] R. Tuinier, J. K. G. Dhont, and T.-H. Fan, How depletion affects sphere motion through solutions containing macromolecules, Europhys. Lett. **75**, 929 (2006).
[61] T.-H. Fan, J. K. G. Dhont, and R. Tuinier, Motion of a sphere through a polymer solution, Phys. Rev. E **75**, 011803 (2007).
[62] T.-H. Fan, B. Xie, and R. Tuinier, Asymptotic analysis of tracer diffusivity in nonadsorbing polymer solutions, Phys. Rev. E **76**, 051405 (2007).
[63] R. Tuinier and T.-H. Fan, Scaling of nanoparticle retardation in semi-dilute polymer solutions, Soft Matter **4**, 254 (2008).
[64] T.-H. Fan and R. Tuinier, Hydrodynamic interaction of two colloids in nonadsorbing polymer solutions, Soft Matter **6**, 647 (2010).
[65] A. Ochab-Marcinek and R. Hołyst, Scale-dependent diffusion of spheres in solutions of flexible and rigid polymers: Mean square displacement and autocorrelation function for FCS and DLS measurements, Soft Matter **7**, 7366 (2011).
[66] L.-H. Cai, S. Panyukov, and M. Rubinstein, Mobility of nonsticky nanoparticles in polymer liquids, Macromolecules (Washington, DC, US) **44**, 7853 (2011).
[67] A. Ochab-Marcinek, S. A. Wieczorek, N. Ziebacz, and R. Hołyst, The effect of depletion layer on diffusion of nanoparticles in solutions of flexible and polydisperse polymers, Soft Matter **8**, 11173 (2012).
[68] Th. F. Tadros, Correlation of viscoelastic properties of stable and flocculated suspensions with their interparticle interactions, Adv. Colloid Interface Sci. **68**, 97 (1996).
[69] W. Wolthers, M. H. G. Duits, D. van den Ende, and J. Mellema, Shear history dependence of the viscosity of aggregated colloidal dispersions, J. Rheol. (Melville, NY, US) **40**, 799 (1996).
[70] J. W. Goodwin and P. A. Reynolds, The rheology of flocculated suspensions, Curr. Opin. Colloid Interface Sci. **3**, 401 (1998).

[71] H. S. Sellers, W. H. Schwarz, M. Sato, and T. Pollard, Boundary effects on the drag of an oscillating sphere: Applications to the magnetic sphere rheometer, J. Non-Newtonian Fluid Mech. **26**, 43 (1987).
[72] K. Sozanski, A. Wisniewska, T. Piasecki, K. Waszczuk, A. Ochab-Marcinek, T. Gotszalkb, and R. Holyst, A depletion layer in polymer solutions at an interface oscillating at the subnano- to submicrometer scale, Soft Matter **10**, 7762 (2014).
[73] T. Taniguchi, Y. Arai, R. Tuinier, and T.-H. Fan, How flow changes polymer depletion in a slit, Eur. Phys. J. E: Soft Matter Biol. Phys. **35**, 88 (2012).
[74] P. G. De Gennes, *Scaling Concepts in Polymer Physics* (Cornell University Press, Ithaca, 1979).
[75] R. B. Bird, R. C. Armstrong, and O. Hassager, *Dynamics of Polymer Liquids* (Wiley-Interscience, 1987), Vol. 1.
[76] T. W. Spriggs, A four-constant model for viscoelastic fluids, Chem. Eng. Sci. **20**, 931 (1965).
[77] P. E. Rouse, A theory of the linear viscoelastic properties of dilute solutions of coiling polymers, J. Chem. Phys. **21**, 1272 (2014).
[78] L. D. Landau and E. M. Lifshitz, *Fluid Mechanics* (Pergamon Press, New York, 1987).
[79] D. Ye, R. Bogner, J.-Q. Li and T.-H. Fan, Dissolution of a colloidal particle in an oscillatory flow, Int. J. Heat Mass Transfer **107**, 489 (2017).
[80] S. Temkin, *Suspension Acoustics: An Introduction to the Physics of Suspensions* (Cambridge Press, New York, 2005).
[81] J. D. Schieber, A. Córdoba, and T. Indei, The analytic solution of Stokes for time-dependent creeping flow around a sphere: Application to linear viscoelasticity as an ingredient for the generalized Stokes-Einstein relation and microrheology analysis, J. Non-Newtonian Fluid Mech. **200**, 3 (2013).
[82] R. Tuinier and H. N. W. Lekkerkerker, Polymer density around a sphere, Macromolecules (Washington, DC, US) **35**, 3312 (2002).
[83] F. Rodriguez, Graphical solution of the Martin equation, Polym Lett Ed. **11**, 485 (1973).
[84] R. Tuinier and T. Taniguchi, Polymer depletion-induced slip near an interface, J. Phys.: Condens. Matter **17**, L9 (2005).
[85] T. Indei, J. D. Schieber, A. Córdoba, and E. Pilyugina, Treating inertia in passive microbead rheology, Phys. Rev. E **85**, 021504 (2012).
[86] S. M. F. D. Syed Mustapha and T. N. Phillips, A dynamic nonlinear regression method for the determination of the discrete relaxation spectrum, J. Phys. D: Appl. Phys. **33**, 1219 (2000).
[87] J.-E. Bae and K. S. Cho, Logarithmic method for continuous relaxation spectrum and comparison with previous methods, J. Rheol. **59**, 1081 (2015).
[88] J. B. Freund and R. H. Ewoldt, Quantitative rheological model selection: Good fits versus credible modes using Bayesian inference, J. Rheol. (Melville, NY, US) **59**, 667 (2015).